Article

Multiple intramolecular triggers converge to preferential G protein coupling in the CB₂R

Adrian Morales-Pastor[1,13], Tamara Miljuš [2,3,4,5,6,13], Miguel Dieguez-Eceolaza [1], Tomasz Maciej Stępniewski[1,7], Vicente Ledesma-Martin[1], Franziska M. Heydenreich [8], Tilman Flock[2], Bianca Plouffe [6,9], Christian Le Gouill [6], Jean Duchaine[6], David A. Sykes [4,10,11], Colin Nicholson[4,10], Eline J. Koers[4,10], Wolfgang Guba[12], Arne C. Rufer [12], Uwe Grether [12], Michel Bouvier [6], Dmitry B. Veprintsev [2,3,4,10] ✉ & Jana Selent [1] ✉

G protein-coupled receptors (GPCRs) are important therapeutic drug targets for a wide range of diseases. Upon activation, GPCRs can initiate several signaling pathways, each with unique therapeutic implications. Therefore, understanding how drugs selectively engage specific signaling pathways becomes paramount. However, achieving this selectivity remains highly challenging. To unravel the underlying multifaceted mechanisms, we integrate systematic mutagenesis of the CB₂R, comprehensive profiling of $G_{\alpha i2}$ and β-arrestin1 engagements and computer simulations to track the effects of mutations on receptor dynamics. Our research reveals multiple triggers within a complex allosteric communication network (ACN) that converge to preferential CB₂R coupling by modulating evolutionarily conserved motifs. Utilizing network path analysis, we find that potent triggers are typically highly connected nodes and are located near regions of high information transmission within the ACN. Our insights highlight the complexity of GPCR signaling and provide a framework for the rational design of drug candidates tailored to evoke specific functional responses, ultimately enhancing the precision and efficacy of therapeutic interventions.

G protein-coupled receptors (GPCRs) are the largest family of cell-surface receptors in humans[1]. They are involved in virtually every physiological process, which makes them invaluable targets for drug development. The cannabinoid receptor 2 (CB₂R) is a GPCR that plays a crucial role in numerous physiological processes, including immune response and inflammation[2]. This makes the CB₂R a promising therapeutic target for a variety of diseases, such as chronic pain, neuroinflammation, and cancer[3,4].

[1]Research Programme on Biomedical Informatics, Hospital del Mar Research Institute and Department of Medicine and Life Science, Universitat Pompeu Fabra, Barcelona, Spain. [2]Laboratory of Biomolecular Research, Paul Scherrer Institute, 5232 Villigen, PSI, Switzerland. [3]Department of Biology, ETH Zürich, 8093 Zürich, Switzerland. [4]Centre of Membrane Proteins and Receptors (COMPARE), University of Birmingham and University of Nottingham, Midlands, UK. [5]Department of Metabolism and Systems Science, College of Medicine and Health, University of Birmingham, Birmingham, UK. [6]Department of Biochemistry and Molecular Medicine, Institute for Research in Immunology and Cancer (IRIC), Université de Montréal, Montréal, Québec, Canada. [7]InterAx Biotech AG, PARK InnovAARE, Villigen, Switzerland. [8]Department of Pharmaceutical Chemistry, University of Marburg, Marburg, Germany. [9]Wellcome-Wolfson Institute for Experimental Medicine, Queen's University Belfast, Belfast, UK. [10]Division of Physiology, Pharmacology & Neuroscience, School of Life Sciences, University of Nottingham, Nottingham, UK. [11]Z7 Biotech Ltd, Nottingham, UK. [12]Roche Innovation Center Basel, F. Hoffmann-La Roche Ltd., Basel 4070, Switzerland. [13]These authors contributed equally: Adrian Morales-Pastor, Tamara Miljuš. ✉e-mail: dmitry.veprintsev@nottingham.ac.uk; jana.selent@upf.edu

Currently, synthetic Δ^9-THC derivatives (e.g. Nabilone[5]) are available for the treatment of chemotherapy-induced nausea and vomits. However, these compounds are non-selective agonists of cannabinoid receptors and may cause psychoactive effects via the CB_1R[4]. Additionally, they can also induce adverse cardiovascular liability in a dose-dependent manner via the CB_1R[6]. In contrast, cannabinoid receptor ligands that do not activate the CB_1R typically lack psychoactive side effects. An example is the FDA-approved phytocannabinoid cannabidiol for the treatment of epilepsy[7] which acts as a negative allosteric modulator of the CB_1R[8] and a partial agonist at the CB_2R[9]. In addition, cannabidiol has been widely used without prescription for the relief of anxiety and stress[10] as well as the management of pain[11] and inflammation[12].

Presently, there are over 20 selective CB_2R agonists in clinical trials for a variety of inflammatory conditions with good safety profiles. Unfortunately, these compounds have not yet been approved, reflecting their elusive therapeutic effect. A potential reason for this is a broad distribution of CB_2R in different tissues, as well as "on demand" engagement of the endocannabinoid system[13], making the development of systemically applied drugs challenging. Developing more pathway-selective drugs represents a promising strategy to modulate the endocannabinoid system with greater precision. An encouraging approach to improve the specificity of drug action as well as modulate its efficacy and to reduce potential side effects, is to exploit the concept of signaling bias. Hereby, a drug preferentially activates specific downstream signaling pathways over ones that are related to unwanted side effects[14–16].

Recent work provides evidence for the relevance of allosteric communication and implicated networks in GPCR function and signaling bias[17,18]. Allosteric communication networks (ACNs) serve as dynamic infrastructure that facilitates communication between remote regions within a GPCR, connecting critical sites like the ligand-binding site to the intracellular effector coupling site. However, the details of how ACNs drive preferential engagement of a specific effector protein remain largely elusive. A main challenge of studying allostery in GPCRs is to monitor ACNs and their alterations related to specific signaling conditions at appropriate spatio-temporal resolution. Molecular dynamics (MD) simulations have emerged as an invaluable tool for complementing static structural, biophysical and biochemical data[19–22] to access the proper resolution levels. They allow for the exploration of protein dynamics at an atomic level, offering insights into the conformational changes at microsecond timescale and corresponding intramolecular networks under conditions of signaling bias[23,24]. Knowledge of the amino acid networks involved in this allosteric communication can not only advance our understanding of GPCR signaling bias but also boost the design of biased ligands with a more precise therapeutic profile.

In this study, we dissect the allosteric communication networks in the CB_2R, combining high-throughput state-of-the-art computational and cell-based assay methods. In a systematic study, we first probe the perturbation of each individual residue within the primary structure of the CB_2R through mutagenesis combined with G protein activation and β-arrestin1 (βarr_1) recruitment. This information is integrated with time-resolved molecular dynamics of the mutation-induced alteration of the CB_2R ACNs using a machine learning pipeline. Most importantly, our study highlights multiple molecular mechanisms and how they interact with the main communication channels between the orthosteric ligand binding site and the intracellular effector binding interfaces via highly conserved residues. Of interest, mutations that preferentially trigger G protein coupling show high connectivity and are typically located closer to ligand-stabilized communication channels of high information transmission. These insights have important implications for the rational development of novel biased ligands targeting not only the orthosteric site

but also allosteric sites in the CB_2R with a therapeutic potential to treat inflammation and pain.

Results

Mutant position and sequence conservation impacts receptor cell-surface expression

First, we analyzed how a mutation in each residue position impacts cell-surface expression. To investigate this, we generated 360 mutants changing the corresponding amino acid to alanine or valine if the amino acid was originally an alanine (see Supplementary Data 1, Fig. 1A–C). We find that approximately 60% of all mutants exhibit a cell-surface expression within the wild-type (WT)-like range (i.e., 80% to 120% of WT expression) (Fig. 1B). This finding suggests that most residue positions in CB_2R display remarkable resilience in maintaining their cell-surface expression upon mutation to alanine/valine. Interestingly, approximately 30% of the mutants show a decrease in expression below the WT-like level, while only 10% of the mutants display an increase (Fig. 1B). This observation indicates that expression-impacting mutants in the CB_2R predominantly reduce cell-surface expression rather than increasing it. Such an effect can be attributed to mutation-induced misfolding and subsequent sequestration in the endoplasmic reticulum or the Golgi complex[25].

Of note, the distribution of expression groups across the receptor sequence reveals an interesting pattern (Fig. 1A). Mutations that result in high CB_2R expression levels tend to be preferentially located in transmembrane domains (TMs) 2 and 3 (yellow circles). On the other hand, mutants associated with low expression (red circles) are more evenly dispersed throughout the transmembrane core of the protein, with fewer occurrences in TM2 and TM3. This spatial association between expression groups suggests a potential functional significance of these specific transmembrane domains in modulating cell-surface expression levels in CB_2R.

Furthermore, we studied the relationship between sequence conservation and cell-surface expression. The sequence conservation in the CB_2R was computed based on the Jensen-Shannon Divergence (JSD) scoring method[26] from a class A human GPCR alignment obtained from GPCRdb[27]. We observe that residues with lower conservation scores (<0.2) show less impact on cell-surface expression, with most mutants belonging to the WT-like group (gray points, Fig. 1C). In contrast, residues with conservation scores > 0.2 yield larger expression deviations compared to the WT (arrows). This finding supports the widely accepted viewpoint that highly conserved residues are crucial for vital receptor functions, such as protein folding or trafficking to the cell membrane. Of interest are also residues that, despite being highly conserved (conservation score > 0.4), show a WT-like expression level upon mutation (gray points). Those residues are likely involved in relevant receptor functions other than cell-surface expression, e.g., ligand binding, coupling to transducer proteins or signal transduction.

Low mutational resilience of βarr_1 recruitment results in preferential $G_{\alpha i2}$ coupling

We also systematically assessed the effect of 360 point mutations within the CB_2R on both $G_{\alpha i2}$ coupling and βarr_1 recruitment after stimulation with the agonist HU-210 using the ebBRET-based Effector Membrane Translocation Assay (EMTA) biosensor platform (Supplementary Data 1). Briefly, receptor-mediated $G_{\alpha i2}$ activation was monitored through the translocation of a downstream effector Rap1GAP subunit to the plasma membrane, where it selectively interacts with activated $G_{i/o}$ protein subfamily[28]. The same plasma membrane translocation principle is used to measure βarr_1 recruitment to the receptor[25]. Supplementary Data 4 shows BRET response scores of the simulated mutants.

For this large-scale analysis, we decided to focus on cases with a marked impact on coupling, i.e., the loss of $G_{\alpha i2}$ or βarr_1 engagement or
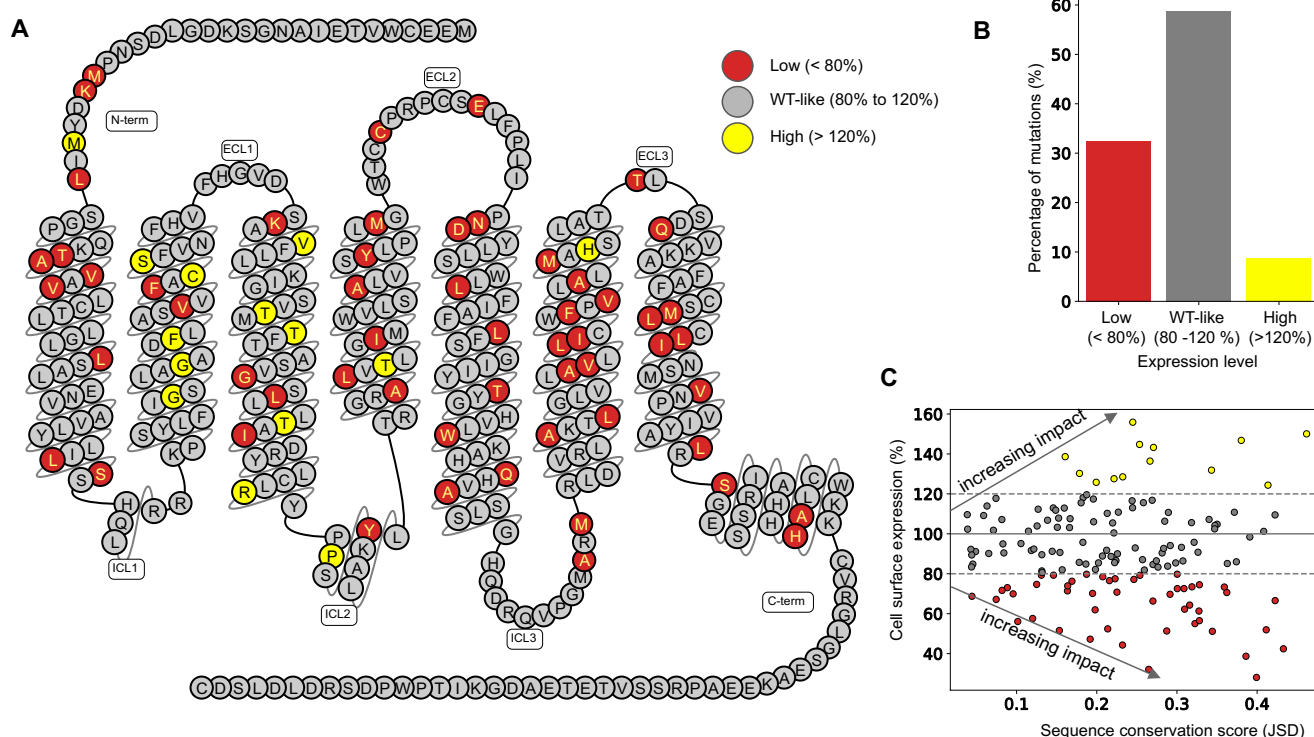
Fig. 1 | **Cell surface expression of 360 CB$_2$R mutants. A** CB$_2$R snake plot showing the distribution of mutants with low, WT-like, and high surface expression. These categories correspond to less than 80% (red), between 80% and 120% (gray), and more than 120% (yellow) of the wild-type expression level. **B** Barplot showing the distribution of the three expression categories: low, WT-like and high.
C Relationship between evolutionary conservation of a residue and its impact on cell-surface expression upon mutation. The conservation score (Jensen-Shannon divergence) was computed for all residues within class A GPCRs. Residues with low conservation scores have the least effect on cell-surface expression, whereas high conservation scores can significantly impact cell-surface expression. Gray arrows indicate the increasing impact. WT surface expression level (100%) is shown with a solid horizontal gray line, while the two gray dashed lines delimit the boundaries of the WT-like expression level. Source data are provided as a Source Data file.

both to obtain meaningful results. We defined four classes of receptor mutants (Fig. 2A, see methods): (i) preferential G$_{\alpha i2}$ coupling (PrefCoup$_{G\alpha i2}$): no measurable βarr$_1$ recruitment but preserved G$_{\alpha i2}$ coupling (Emax > 50%), (ii) preferential βarr$_1$ recruitment (PrefCoup$_{\beta arr1}$): no measurable G$_{\alpha i2}$ coupling but preserved βarr$_1$ recruitment (Emax > 50%), (iii) loss of receptor function (NoCoup$_{G\alpha i2\_\beta arr1}$): no measurable signal for G$_{\alpha i2}$ nor βarr$_1$ and finally (iv) preserved coupling (Coup$_{G\alpha i2\_\beta arr1}$): mutations that preserve G$_{\alpha i2}$ coupling and βarr$_1$ recruitment with an Emax > 50%. Using this classification, we observe that 70% of mutants preserve coupling properties (Emax > 50%) to G$_{\alpha i2}$ and βarr$_1$, whereas 30% result in a loss of G$_{\alpha i2}$, βarr$_1$ or both (Fig. 2B, Supplementary Fig. 1). Interestingly, our data indicate that coupling-impaired mutants predominantly induce the loss of βarr$_1$ recruitment (19%), leading to preferential G$_{\alpha i2}$ coupling, whereas G$_{\alpha i2}$ coupling seems to be more robust to mutational alterations (only 2% specifically abrogated G$_{\alpha i2}$ activation).

To investigate whether a loss of βarr$_1$ recruitment is correlated with a decrease in G$_{\alpha i2}$ coupling, we plotted the G$_{\alpha i}$ efficacy (Emax$_{Gi}$) distribution for mutants with impaired βarr$_1$ recruitment (i.e., PrefCoup$_{G\alpha i2}$ mutants) (Fig. 2C). The plot reveals that PrefCoup$_{G\alpha i2}$ mutants exhibit G$_{\alpha i}$ efficacies that are normally distributed around the WT level (Fig. 2C), suggesting that abolishment of βarr$_1$ recruitment does not necessarily affect the efficacy of G protein signaling. Of note, there is also a significant fraction of receptor mutants (12%) incapable of coupling to both G$_{\alpha i}$ and βarr$_1$ (Fig. 2B). These impactful mutations are enriched in highly conserved regions (e.g., microswitches, highlighted with a black circle, Fig. 2A) and represent approximately 50% of highly conserved residues (Fig. 2D).

To obtain a more comprehensive understanding of the implication of residue conservation for receptor functionality, we plotted its

distribution for mutants with preserved G$_{\alpha i2}$ and βarr$_1$ coupling (Coup$_{G\alpha i2\_\beta arr1}$) compared to the ones with preferential G$_{\alpha i2}$ coupling (PrefCoup$_{G\alpha i2}$). To exclude a potential impact through differential receptor expression level, we only plot mutations with a WT-like expression level (i.e., 80% to 120%). We find that PrefCoup$_{G\alpha i2}$ mutants (orange line, Fig. 2E) show a clear shift toward higher conservation scores compared to Coup$_{G\alpha i2\_\beta arr1}$ mutants (blue line, Fig. 2E). Interestingly, the PrefCoup$_{G\alpha i2}$ mutant distribution shows a bimodal behavior pointing to the existence of two populations. One population is similar to the Coup$_{G\alpha i2\_\beta arr1}$ mutant distribution with a peak at a conservation score of 0.2 and a second population that is shifted to higher scores with a peak at 0.42. Our data highlight the relationship between the evolutionary conservation of a residue and its impact on the receptor coupling preference.

Preferential G$_{\alpha i2}$-coupled mutants are located in proximity to network connections with high information transmission

We hypothesize that the receptor dynamics and the stabilization of specific receptor states through an allosteric communication network (ACN) are crucial for the functional response of the CB$_2$R. In this framework, PrefCoup$_{G\alpha i2}$ mutants likely exert their effects by perturbing the allosteric communication network in the CB$_2$R compared to mutants with preserved coupling to G$_{\alpha i2}$ and βarr$_1$ (Coup$_{G\alpha i2\_\beta arr1}$).

To test this hypothesis, we performed all-atom molecular dynamics (MD) simulations and sampled the ACN for the WT CB$_2$R (WT ACN) in complex with the agonist HU-210 over 2 μs accumulated simulation time (5 × 400 ns). The ACN is computed based on contact frequencies including hydrophobic interactions, hydrogen bonds and water-mediated interactions. Then we identified the 100 shortest pathways on this network (LigACN) that mediate the communication
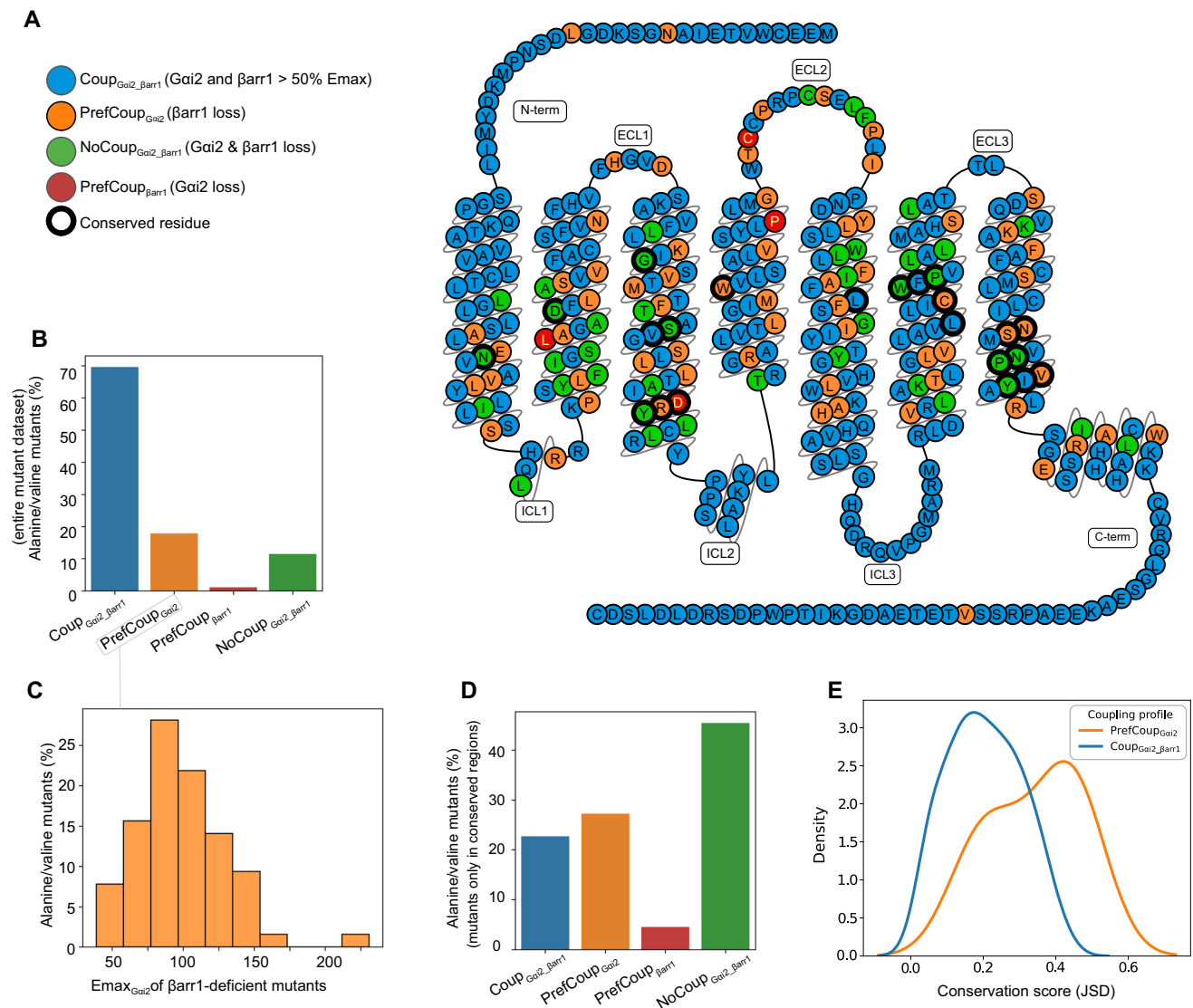
Fig. 2 | Induced coupling profiles by CB$_2$R mutants. A Location of mutations in the CB$_2$R classified on a snake plot as: Coup$_{Gαi2\_βarr1}$: preserved G$_{αi2}$ and βarr$_1$ coupling (blue), PrefCoup$_{Gαi2}$: preferential G$_{αi2}$ coupling through a loss of βarr$_1$ recruitment (orange), PrefCoup$_{βarr1}$: preferential βarr$_1$ recruitment through loss of G$_{αi2}$ coupling (red), and NoCoup$_{Gαi2\_βarr1}$: G$_{αi2}$ and βarr$_1$ couplings are lost (green). Bold outlined positions indicate highly conserved residues/microswitches such as NPxxY, CWxP, etc. **B** Distribution of coupling profiles classes (see also scatter plot in Supplementary Fig. 1). **C** Emax distribution for CB$_2$R mutants with a preferential G$_{αi2}$ coupling profile. The Emax distribution resembles a normal distribution which is confirmed by a two-side D'Agostino and Pearson's test[74] (p-value = 4.89 E^{-05},

sample size: n = 64 βarr$_1$ deficient mutants). **D** Distribution of coupling profiles for mutants in conserved regions. Percentages differ considerably from the ones of the full set of mutants in (Fig. 2B). **E** Kernel density estimation of the distribution of conservation scores among PrefCoup$_{Gαi2}$ mutants and Coup$_{Gαi2\_βarr1}$ mutants with a WT-like expression level (80% to 100%) showing a clear shift between both densities. The statistical significance of this shift is confirmed using a one-side Kolmogorov–Smirnov test[75] (p-value of 0.07, sample size: n = 64 PrefCoup$_{Gαi2}$ and 251 Coup$_{Gαi2\_βarr1}$ mutants). A conservation score distribution for all coupling classes can be found in Supplementary Fig. 11. Source data are provided as a Source data file.

from the orthosteric ligand binding site to the intracellular coupling site (Fig. 3A). To estimate information transmission of a contact in the ACN, we computed the frequency of their appearance in 100 shortest pathways (see methods, Fig. 3A, B, and Supplementary Data 3 for transmission information computed as degeneracy for 35 simulated mutants). For our interpretation, we treat the LigACN as the principal contact network, which is stabilized by the ligand to promote a specific receptor state and functional response. In contrast, the entire WT ACN encompasses the complete allosteric connectivity within CB$_2$R and provides valuable insights into connections that link remote receptor regions to the LigACN. These connections represent a resource that can be harnessed by allosteric modulators, including membrane lipids, small molecules, or other interacting proteins, to fine-tune receptor conformational states and, consequently, modulate its response.

A first inspection of the LigACN stabilized by agonist HU-210 shows that it comprises several residues crucial for receptor function, known as conserved microswitches (Fig. 3A). These microswitches include residue R131^{3x50} from the DRY motif, residue N291^{7x45} and S292^{7x46} in the sodium binding site, and all five residues in the NPxxY motif N295^{7x49} to Y299^{7x53} (the GPCRdb numbering scheme is used[29]). The presence of these highly conserved residues within the LigACN strongly supports its relevance in transmitting information and maintaining the protein's function. Furthermore, we find that the LigACN elicits a strong communication through the upper and lower part of TM7 as well as the lower parts of TM2, 6 and 3.

We then determined the distance of PrefCoup$_{Gαi2}$ mutants to the top connections with high information transmission in the LigACN (LigACN$_{top}$, see method section) (Fig. 3C). Interestingly, we find that
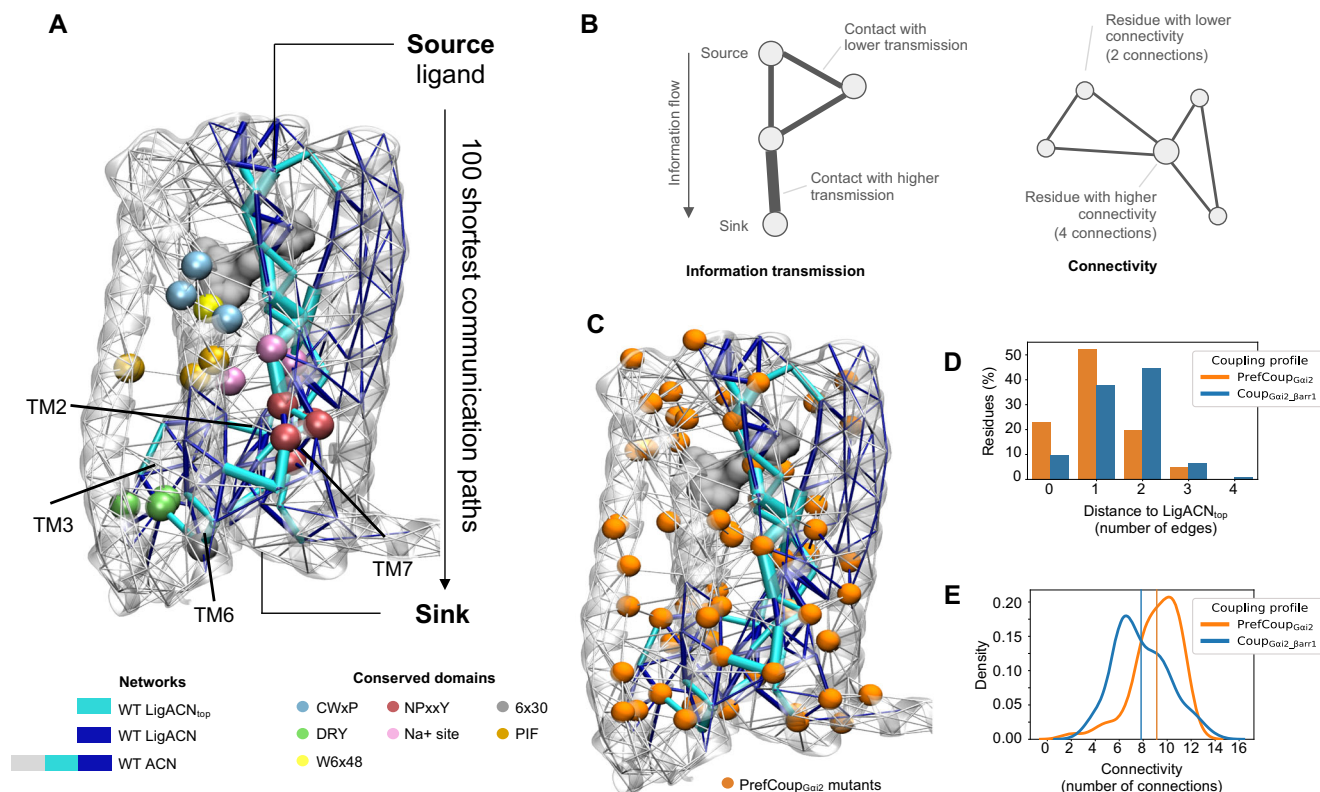
Fig. 3 | The allosteric communication network in the WT CB$_2$R. A Depiction of the entire allosteric communication network in the inactive WT CB$_2$R (WT ACN) (PDB ID: 6KPC[32]). The WT ACN encompasses the ligand-stabilized ACN (LigACN, dark blue) and their top connections with high information transmission (LigACN$_{top}$, light blue). The thickness of the contacts is proportional to their information transmission between the ligand and the intracellular receptor site (see Methods). **B** Schematic illustration of information transmission and the connectivity of a specific node in the network. **C** PrefCoup$_{G\alpha i2}$ mutants are shown as orange spheres alongside the LigACN and its top connections (LigACN$_{top}$) on the inactive CB$_2$R structure (PDB ID: 6KPC[32]). **D** Distance of PrefCoup$_{G\alpha i2}$ and Coup$_{G\alpha i2\_\beta arr1}$ mutants to the LigACN$_{top}$. The distance is represented as the number of edges from a mutation position to the LigACN$_{top}$ (x-axis). The percentage of

mutants at a given distance is provided (y-axis). Note that the plotted distance profile depends on the cutoff for the information transmission that defines the LigACN$_{top}$ (cutoff for top connections: 0.146). To confirm that the described tendency holds true also for different cutoffs values, we provide distribution plots in Supplementary Fig. 14. **E** Connectivity distribution plot of PrefCoup$_{G\alpha i2}$ mutants (orange) and Coup$_{G\alpha i2\_\beta arr1}$ (blue). Connectivity for each residue position is computed as the number of connections in the network (see Fig. 3B). Vertical lines indicate the mean value of each distribution. Statistical analysis between PrefCoup$_{G\alpha i2}$ and Coup$_{G\alpha i2\_\beta arr1}$ mutants was performed using one-side Student's t-test (*$p < 0.001$, sample size: $n = 14$ PrefCoup$_{G\alpha i2}$ and 20 Coup$_{G\alpha i2\_\beta arr1}$ mutants). Source data are provided as a Source Data file.

PrefCoup$_{G\alpha i2}$ mutants are present closer to the LigACN$_{top}$ (i.e., 0 to 1 connection, Fig. 3D) whereas Coup$_{G\alpha i2\_\beta arr1}$ mutants are located at larger distances (2 to 4 edges). We verified that this closeness was statistically significant by comparing its mean value to a null distribution built using random sets of residues (p-value 0.006). On top of this proximity, inspection of the protein contact network revealed that PrefCoup$_{G\alpha i2}$ mutants on average have higher connectivity (i.e., a residue has more connections to other residues) than Coup$_{G\alpha i2\_\beta arr1}$ mutants (Fig. 3B, E). Both proximity to highly information-transmissive connections in the LigACN and the higher connectivity rationalize why these residues have a significant functional impact on the receptor's coupling profile.

Multiple molecular mechanisms initiate G$_{\alpha i2}$ preferential coupling

To obtain a deeper mechanistic understanding of changes in the ACN that drive preferential G$_{\alpha i2}$ coupling as a result of the loss of βarr$_1$ recruitment, we carried out additional MD simulations of a set of 34 mutants from the 360 point mutations including 14 PrefCoup$_{G\alpha i2}$ mutants, 20 Coup$_{G\alpha i2\_\beta arr1}$ and the wild type, which belongs to Coup$_{G\alpha i2\_\beta arr1}$ (Fig. 4A, Supplementary Table 1). The selection of mutants was done based on two criteria: (1) mutants show WT-like expression levels, as a reduced/increased receptor expression can significantly alter receptor signaling[30] and (2) mutants are located in

receptor regions that are structurally resolved. With the aim to understand the initial ACN re-arrangements for preferential G$_{\alpha i2}$ coupling as a result of βarr$_1$ loss, we started from an inactive receptor state (PDB ID 5ZTY[31], see "Methods" section). For each simulated mutant, we monitored the dynamics of formation and disruption for different interaction types within the entire receptor contact network. The interaction stability for thousands of interatomic connections was quantified by computing the contact frequency for the last 400 ns in 5 replicates (i.e., 2 µs total analysis time per mutant) (Fig. 4B).

First, we investigated if PrefCoup$_{G\alpha i2}$ mutants induce alterations in the ligand-stabilized ACNs. In fact, we find that individual PrefCoup$_{G\alpha i2}$ mutants typically induce larger LigACNs compared to Coup$_{G\alpha i2\_\beta arr1}$ mutants, i.e., increase the number of nodes in the pathways from the ligand to the intracellular receptor site (Fig. 4C). It seems that PrefCoup$_{G\alpha i2}$ mutants disrupt information transmission pipelines in the WT LigACN. This disruption leads to a branching of the information flow along longer pathways including more residue nodes, likely resulting in a less efficient transmission of information. The functional readout of those mutants suggests that the inclusion of more residues in the communication pipeline and in turn less efficient information transmission is linked to a loss of β-arrestin recruitment in the CB$_2$R.

To extract further structural information relevant for preferential CB$_2$R coupling, we reduced the dimensionality of simulated contact
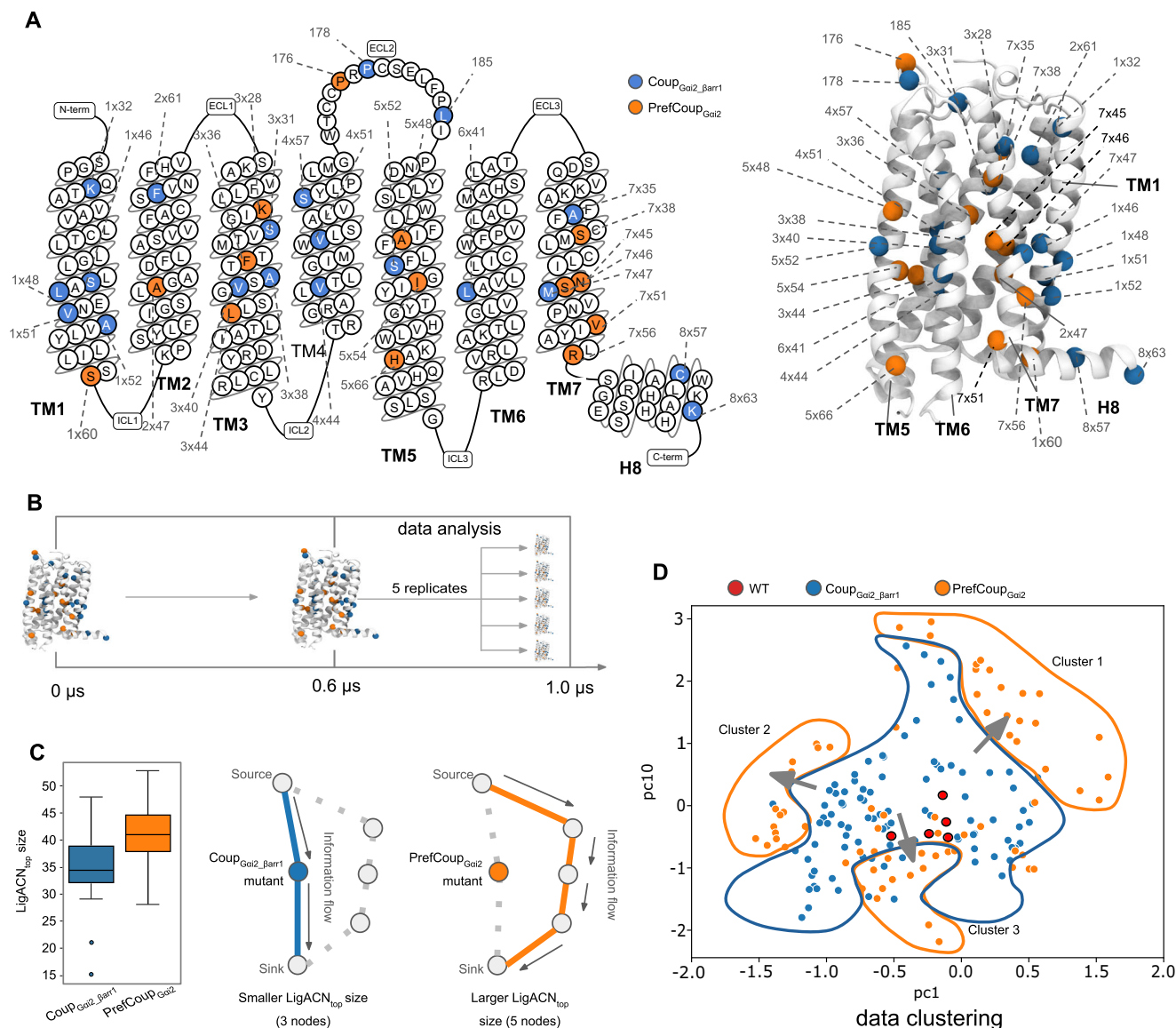
Fig. 4 | MD-based classification of PrefCoup$_{G\alpha i2}$ and Coup$_{G\alpha i2\_\beta arr1}$ mutants.
A Location of simulated mutants and their coupling profiles shown on a snake plot (left) and the CB$_2$R structure (right). PrefCoup$_{G\alpha i2}$ mutants are shown in orange and Coup$_{G\alpha i2\_\beta arr1}$ in blue (PDB ID: 6KPC). **B** MD simulations scheme: the initial system was simulated in production conditions for 0.6 μs. After that, 5 replicates were respawned applying random perturbations to the atom speeds. These 5 replicates were evolved for further 0.4 μs reaching a total evolution time of 1 μs. This yields a total simulation time of 2.6 μs per mutant. The respawned replicates (5 × 0.4 μs) are used for data analysis. **C** Distribution plot of the network size of LigACNs (i.e., number of nodes) for PrefCoup$_{G\alpha i2}$ mutants compared to WT and Coup$_{G\alpha i2\_\beta arr1}$ mutants. The data for LigACNs including interatomic contacts in the ACN for all 34 mutants and the wild type is found in Supplementary Data 2. The center line in boxplots represents the median while the box boundaries extend from the first (25%) and third (75%) quartile, representing the interquartile range (IQR). Boxplot whiskers extend to 1.5*IQR and outliers are represented as points. Schematic representations illustrate the impact of a mutation on the LigACN$_{top}$ size.
D Principal Component Analysis (PCA) of MD data using contact frequencies for 10 different contact types: 3 types of hydrogen bonds, salt bridges, Pi-cation, Pi-stacking, T-stacking, Van der Waals including hydrophobic interactions, water bridges, extended water bridges. The best-performing PC plane for separating Coup$_{G\alpha i2\_\beta arr1}$ and PrefCoup$_{G\alpha i2}$ is PC1 versus PC10, selected using a Support Vector Classifier (SVC). The SVC model (blue contour line) encompasses the Coup$_{G\alpha i2\_\beta arr1}$ mutants in the middle of the plane and three different clusters for the PrefCoup$_{G\alpha i2}$ mutants (orange line) at peripheral regions. The WT control simulations are highlighted in red. Source data are provided as a Source data file.

networks by applying principal component analysis (PCA) and selected the best performing principal component (PC) using a Support Vector Classifier (SVC). Interestingly, projecting the data on a PC plane defined by PC1 and PC10 reveals a separation of Coup$_{G\alpha i2\_\beta arr1}$ mutants (blue points) and the PrefCoup$_{G\alpha i2}$ mutants (orange points). In other words, preferential G$_{\alpha i2}$ coupling and loss of βarr$_1$ recruitment in our dataset is described by one PC (PC1) with high explained variability (13%) and a second PC (PC10) with less explained variability (3%). Apparently, there are also contacts with high variability (i.e., PC2 to 9) that are not related to preferential G$_{\alpha i2}$ coupling in the CB$_2$R and that

could be linked to other receptor functions. This could include protein folding, trafficking, post-translational modifications, receptor dimerization, as well as interactions with other coupling partners such as kinases (e.g., GRKs), RGS proteins, Filamin A, calmodulin or other natural allosteric modulators like lipid molecules and ions. These interactions enable the CB$_2$R to mediate its full range of physiological effects.

Interestingly, the spreading of the mutants that preserve coupling (Coup$_{G\alpha i2\_\beta arr1}$, blue points) around the true WT system (red points) indicates that some variability in the contact network is tolerated for
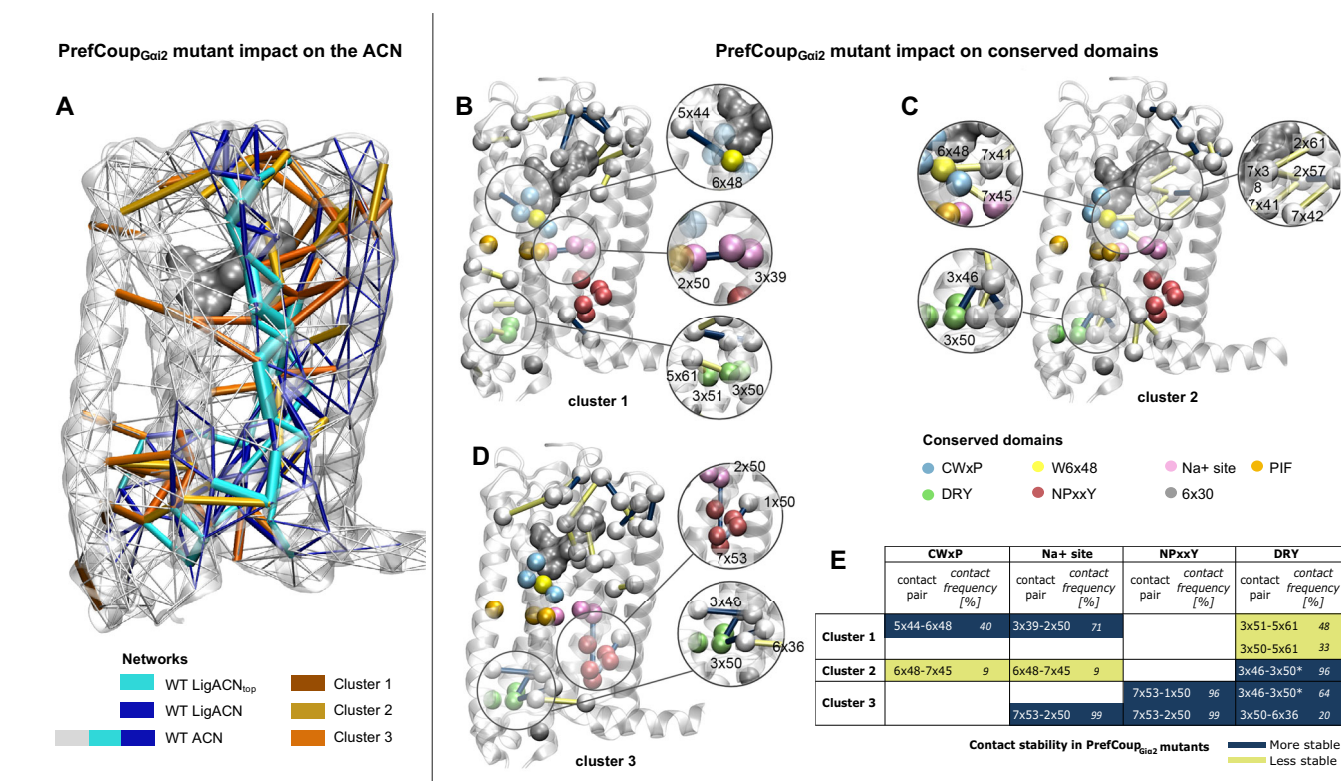
PrefCoup$_{G\alpha i2}$ mutant impact on the ACN

A

PrefCoup$_{G\alpha i2}$ mutant impact on conserved domains

B

cluster 1

C

cluster 2

D

cluster 3

Networks
- WT LigACN$_{top}$ — Cluster 1
- WT LigACN — Cluster 2
- WT ACN — Cluster 3

Conserved domains
- CWxP — W6x48 — Na+ site — PIF
- DRY — NPxxY — 6x30

E

	CWxP		Na+ site		NPxxY		DRY	
	contact pair	*contact frequency [%]*	contact pair	*contact frequency [%]*	contact pair	*contact frequency [%]*	contact pair	*contact frequency [%]*
Cluster 1	5x44-6x48	*40*	3x39-2x50	*71*			3x51-5x61	*48*
							3x50-5x61	*33*
Cluster 2	6x48-7x45	*9*	6x48-7x45	*9*			3x46-3x50*	*96*
Cluster 3					7x53-1x50	*96*	3x46-3x50*	*64*
			7x53-2x50	*99*	7x53-2x50	*99*	3x50-6x36	*20*

Contact stability in PrefCoup$_{G\alpha i2}$ mutants — More stable / Less stable

Fig. 5 | Structural characterization of PrefCoup$_{G\alpha i2}$ mutant clusters.
A Perturbation map of the ACN induced by PrefCoup$_{G\alpha i2}$ mutants. Top interaction features for PrefCoup$_{G\alpha i2}$ cluster 1 (dark brown), 2 (light brown) and 3 (orange). The interactions are plotted together with the computed ACNs for the WT CB$_2$R. For instance, such depiction highlights allosteric connections (brown to orange) to the ligand-stabilized ACN (light and dark blue) that are perturbed in preferential G$_{\alpha i2}$ coupling of the CB$_2$R (PDB ID: 6KPC). **B**–**D** Mutant impact on highly conserved receptor regions for clusters 1 to 3. Non-conserved residues which are part of the modulation are represented as white spheres whereas the corresponding contact is highlighted as a cylinder indicating the change of contact stability compared to conserved coupling (Coup$_{G\alpha i2\_\beta arr1}$): navy blue corresponds to increased interaction stability in the PrefCoup$_{G\alpha i2}$ mutants, yellow indicates decreased interaction

stability. The thickness of the cylinders is proportional to the absolute value of the coefficient for that interaction in the logistic regression model (PDB ID: 6KPC). **E** Summary of mutant-perturbed domains of high conservation (i.e., CWxP, Na+ site, NPxxY, DRY) for PrefCoup$_{G\alpha i2}$ mutant clusters 1 to 3. For each cell, we indicate the implicated residues in the contact and the corresponding contact frequency for each pair of residues. Each cell is colored according to the prediction of a logistic regression model: more stable contacts (navy blue) and less stable contacts (yellow) of PrefCoup$_{G\alpha i2}$ compared to Coup$_{G\alpha i2\_\beta arr1}$ mutants. Further details about differences in contact frequencies between PrefCoup$_{G\alpha i2}$ and Coup$_{G\alpha i2\_\beta arr1}$ mutants are plotted in Supplementary Fig. 5. Source data are provided as a Source data file.

preserving coupling with an Emax > 50%. Intriguingly, we find that PrefCoup$_{G\alpha i2}$ mutants (orange points) tend to shift further away from the true WT center (red points) (Fig. 4D). Apparently, these mutations perturb specific elements (i.e., stabilization or destabilization) in the contact networks that fall outside the tolerated region of the Coup$_{G\alpha i2\_\beta arr1}$ mutants (blue points). In addition, we find that PrefCoup$_{G\alpha i2}$ mutants move in three different directions forming clusters 1 to 3. Hence, each cluster appears to differently disrupt the contact network, leading to impaired βarr$_1$ recruitment and preferential G$_{\alpha i2}$ coupling. Ultimately, this suggests that different mechanisms are implicated in preferential G$_{\alpha i2}$ coupling and the loss of βarr$_1$ recruitment in the CB$_2$R. This could also explain why some PrefCoup$_{G\alpha i2}$ mutants fall within the blue cluster of preserved coupling as they likely exploit another molecular mechanism that is not projected into the plane of PC1 and PC10.

Furthermore, we observe that the three PrefCoup$_{G\alpha i2}$ clusters (orange points) are located at different distances from the true WT simulations (red points). Specifically, cluster 3 is very close to the true WT simulations compared to clusters 1 and 2. This suggests that cluster 3-specific contact stabilities are more sensitive and smaller network alterations can push the CB$_2$R from a preserved coupling profile to a PrefCoup$_{G\alpha i2}$ profile. The PCA data separation is confirmed using a machine-learning classification approach with a Support Vector Classifier (SVC), which effectively differentiates mutant populations (blue

contour, Fig. 4D). Additionally, K-means clustering analysis further corroborates the presence of three distinct clusters (Supplementary Fig. 2).

Of note, we also simulated the same 34 mutants including 14 PrefCoup$_{G\alpha i2}$ mutants, 20 Coup$_{G\alpha i2\_\beta arr1}$ and the wild type, which belongs to Coup$_{G\alpha i2\_\beta arr1}$ in the active CB$_2$R structure coupled to the G$_\alpha$ subunit (PDB ID 6KPF[32]). Interestingly, we were not able to obtain conclusive results discriminating PrefCoup$_{G\alpha i2}$ from the Coup$_{G\alpha i2\_\beta arr1}$ profile (Supplementary Fig. 3). A possible reason for this is that G protein binding to the CB$_2$R and its penetration into the receptor core disrupts many intramolecular contacts within the allosteric contact network as TM helices move apart (Supplementary Fig. 4). This in turn reduces the measurable impact of mutants on the contact network within CB$_2$R.

Contact alterations in conserved molecular switches are involved in G$_{\alpha i2}$ preferential coupling
To capture in more detail the structural and dynamic alterations in the receptor contact network that lead to G$_{\alpha i2}$ preferential coupling, we fitted a logistic regression for each PrefCoup$_{G\alpha i2}$ cluster to separate them from the Coup$_{G\alpha i2\_\beta arr1}$ group (see method). Top interaction features (orange color scaled connections) that distinguish preferential G$_{\alpha i2}$ from the preserved coupling profile are plotted on the allosteric communication network (WT ACN, gray), including the

ligand-stabilized ACN (cyan) (Fig. 5A). The obtained representation indicates that mutational perturbation in preferential $G_{\alpha i2}$ coupling for clusters 1 to 3 (orange color scale) involves a complex and multifaceted modulation of the WT ACN (gray plus cyan) and the corresponding LigACN (cyan). To further simplify the interpretation of these complex perturbations of the WT ACN, we focus on highly conserved receptor regions with known relevance for receptor function, such as the CWxP motif, allosteric sodium binding site, NPxxY motif, and the DRY motif. Cluster-specific modulations are depicted in Fig. 5B–D (detailed structural description can be found in Supplementary Note 1). A cluster summary (Fig. 5E) reveals that the sodium binding site and the DRY motif are modulated in all three identified clusters, the CWxP only in clusters 1 and 2, and the NPxxY motif only in cluster 3. Based on the finding that the DRY motif and the sodium binding site are modulated in all three PrefCoup$_{G_{\alpha i2}}$ clusters, it is tempting to speculate that they play a critical role in preserving βarr_1 recruitment. The observed modulation of those motifs occurs indirectly through mutational perturbations from topologically different sites. Unfortunately, we could not assess the direct impact of those motifs on preferential CB_2R coupling as their mutation dramatically impacts receptor expression (see Supplementary Data 1). Another interesting observation is that detected perturbations around the sodium binding site, CWxP and DRY motifs involve contact (de)stabilization effects through different residues (Fig. 5E, Supplementary Fig. 5). This corroborates the finding that multiple molecular mechanisms can converge into the same receptor response, i.e., loss of βarr_1 recruitment while preserving $G_{\alpha i2}$ coupling with an Emax > 50%.

Discussion

Allosteric communication networks are highly complex dynamic entities that drive receptor conformational states and in turn determine their final functional outcome as a response to environmental changes (e.g., mutations or ligand stimulation). Here, we investigated the dynamics of such networks and their modulation related to preferential signaling of the CB_2R. The results obtained from our study shed light on several key aspects that link receptor structure and dynamics to function. We anticipate that our findings will provide a broadly applicable framework for understanding CB_2R function due to the integration of large-scale experimental data (a systematic mutational scan of CB_2R) with computational data (MD simulations of all CB_2R mutants retaining WT-like expression levels). Additionally, the use of graph theory analysis and machine learning-based classification enhances the generalizability of our approach.

First of all, our functional readouts suggest that $G_{\alpha i2}$ coupling is more robust to mutational perturbations compared to βarr_1 recruitment in the CB_2R (Fig. 2B). Our observation is in line with a similar study on β_2 adrenergic receptor (β_2AR) where more than 75% of mutational substitutions retain the receptor's G protein coupling profile[33]. However, it is important to mention that this is not a general tendency for GPCRs, as shown recently for the angiotensin II type 1 receptor (AT_1R)[18]. For this receptor, β-arrestin recruitment is more resistant to mutations compared to G protein binding. This could possibly be related to the intrinsic propensity of GPCRs to differentially engage in interactions with β-arrestins. While class A GPCRs for arrestin recruitment (such as β_2AR and CB_2R) interact with arrestins only transiently, class B receptors (V_2R and AT_1R) form more stable interactions which are potentially more resistant to disruptions by single-point mutagenesis[34].

Plotting the $G_{\alpha i2}$ preferential mutants on the static CB_2R structure offers a glimpse into their potential impact based on their location within the receptor (Fig. 2A). Interestingly, mutations that impact β-arrestin recruitment are mainly found in transmembrane helices and only one was found in the receptor C-terminal tail (expanded discussion in Supplementary Note 2). This might be surprising as serine and threonine residues in intracellular regions are known to promote

arrestin recruitment upon GRK-mediated phosphorylation. However, this result can be attributed to the ability of CB_2R to recruit arrestin independently of GRK phosphorylation, as previously reported[35]. We further confirmed this finding using GRK2/3/5/6 knockout cell lines (Supplementary Fig. 6).

Although static representations can be informative, they fall short when studying the molecular mechanism that drives the modulation of a receptor that is in constant motion. Here, we demonstrate that the intrinsic CB_2R flexibility can be captured with atomistic resolution through allosteric communication networks within the receptor in which each interatomic connection is characterized through a distinct contact frequency. Further network processing using graph theory highlights how the agonist HU-210 allosterically communicates with the intracellular coupling site of the CB_2R mainly through TM7 (Fig. 3A). The relevance of TM7-related agonist binding goes along with a previous study for the β_2 adrenergic receptor despite using a different approach. Applying the concept of correlated movements for the detection of allosteric communication pipelines[36], the authors find that the inverse agonist-bound inactive states uses mainly TM6, whereas agonists-bound active states favor TM7 as the main communication pipeline.

Investigating the mutant position, their information transmission and connectivity within such networks reveals a complex modulation of CB_2R coupling (Fig. 3B). For a more detailed description, we introduced the concept of the ligand-stabilized ACN (LigACN) which is part of the overall CB_2R ACN. The LigACN is important for stabilizing the receptor in a specific conformational ensemble and therefore directing the functional outcome of the ligand-stimulated receptor. Importantly, we find that $G_{\alpha i2}$ preferential mutants are located closer to connections of high transmission in the ligand-stabilized ACN (Fig. 3B, C) and are of higher network connectivity (Fig. 3E). From this, we can conclude that both information transmission and connectivity are critical residue properties for modulating the allosteric network in the CB_2R and in turn its ability to recruit βarr_1. Mechanistically, this can be explained as follows: mutant perturbations of allosteric connections (i.e., loosening or strengthening) in the WT ACN and specifically in the LigACN shift the CB_2R conformational ensemble from states with favorable affinities for multiple transducer proteins (e.g., $G_{\alpha i}$, βarr_1, others) to states that lose βarr_1 while preferentially preserving $G_{\alpha i2}$ with Emax > 50% (Supplementary Fig. 7).

Our findings are in line with previous studies of GPCRs[24,37] and other protein classes[38], showing that disruption of allosteric communication networks through mutations results in a significant impact on protein function. This also has implications for allosteric modulators that can fine-tune function by perturbing allosteric connections between different protein regions[39], even from peripheral receptor sites. In this context, the obtained mutational CB_2R map, which resolves each amino acid position and its role for receptor function is highly valuable for identifying novel allosteric sites for drug discovery programs. Nevertheless, it is worth noting that not all mutations occurring within our computed LigACN consistently exhibit the same level of efficiency in altering $G_{\alpha i2}$ preferential coupling. This is not surprising as those positions might be involved in other functional consequences (e.g., coupling to other (un)known signaling partners) that are not taken into account in our study. Further investigations are required to better understand these functional relationships.

Ultimately, the most important finding of our study is related to the observation that there are multiple molecular mechanisms that can induce the same functional response, i.e., preferential $G_{\alpha i2}$ coupling. In fact, this goes along with the applied concept of allosteric communication networks that includes regulatory triggers from different receptor regions. Principal component analysis (Fig. 3D) and logistic regression (Fig. 4) pinpoint three separate mechanisms that regulate highly conserved receptor motifs such as CWxP, sodium binding site,

NPxxY and DRY. The involvement of those microswitches in impairing β-arrestin recruitment has been reported in different individual studies (i.e., DRY motif[39–42], NPxxY motif[43], the toggle switch[44], and the sodium binding site[45]). Importantly, we find that the same molecular switch can be perturbed through different combinations of interactions and contact stabilities as highlighted by our PrefCoup$_{G\alpha i2}$ clusters 1 to 3 (Fig. 5B–D). Ultimately, we anticipate the existence of other molecular mechanisms based on the observation that not all PrefCoup$_{G\alpha i2}$ mutants in our dataset (e.g., S61A at the bottom of TM1) fall into one of the three PrefCoup$_{G\alpha i2}$ clusters, but are located in the preserved signaling cluster (Fig. 3C). Moreover, we expect that additional mechanisms will come into play when changing experimental conditions such as the choice of agonist or the type of mutational substitution (e.g., as occurring in single nucleotide polymorphisms). Given the multitude of molecular mechanisms that induce preferential G$_{\alpha i2}$ coupling suggests that biased ligands may not all operate through a shared universal mechanism. Instead, it is possible that chemically different ligand classes achieve the same bias response by employing distinct structural mechanisms. A key factor in this process will be specific ligand-receptor contacts within the binding pocket, which are unique to each ligand class and which translate into the stabilization of distinct ACNs.

Interestingly, there is experimental evidence that this proposed concept is common for GPCRs. For instance, it has been shown for two chemically different agonists of the δ opioid receptor that their ability to activate G$_{\alpha i}$ is differentially impacted by a N^{7x45}A mutation, a residue that is part of the highly conserved allosteric sodium binding site deep inside the receptor (Supplementary Table 2). Whereas, the peptide agonist DADLE completely loses its ability to activate G$_{\alpha i}$, the agonist BW373U86 maintains its G$_{\alpha i}$ activation properties similar to that of the WT upon a N^{7x45}A mutation. Overall, these findings corroborate that structurally diverse ligands with unique ligand receptor interaction profiles engage distinct ligand-specific networks to achieve the same functional outcome. This has significant implications for drug responses and personalized medicine. For example, a patient harboring a specific genetic variant may respond differently to a treatment depending on whether the variant affects the ligand-specific ACN or not.

In addition to explaining 'diverse ligands with the same functional outcome', our framework also accounts for 'closely related ligands with different functional responses' as observed in monoaminergic receptors. Subtle modifications in the ligand's chemical structure—and consequently ligand-receptor interactions—can convert a natural agonist into a biased agonistst[46–48]. According to our structural framework, this is due to alterations of the stabilized ACNs triggered by the different ligand receptor contacts.

Ultimately, β-arrestin recruitment for many GPCRs depends on GRK-mediated phosphorylation[49] including prototypical receptors such as β$_2$AR[50] and AT$_1$R[51]. Importantly, since CB$_2$R recruits βarr$_1$ independently of GRKs (Supplementary Fig. 6), mutant-induced alterations in the ACNs are unlikely to affect GRK-mediated phosphorylation. Instead, they may impact alternative β-arrestin recruitment mechanisms such as its direct interaction with the receptor core to yield a preferential G protein coupling profile. By delving into these unique mechanisms, we can advance our understanding of biased signaling and target GPCR-mediated signaling pathways more effectively to eventually broaden our repertoire of therapeutic approaches.

In conclusion, our study provides insights into the intricate interplay of multiple triggers on complex allosteric communication networks in the CB$_2$R and their final functional outcomes. Potent triggers of such changes in ACNs that lead to distinct intracellular signaling responses are characterized by high connectivity and their close vicinity to high information-transmissive connections. Our findings have important implications for elaborating drug design strategies aimed at tailoring receptor response towards more efficacious and safer drugs. However, given the complexity of nature and the involvement of multiple molecular mechanisms, further research is necessary to fully comprehend these intricate processes and their potential applications in drug development.

Methods

Plasmids and mutagenesis

Human CB$_2$R gene was optimized for expression in mammalian systems and synthesized (Genewiz). The CB$_2$R gene was fused to an N-terminal signal sequence, SNAP-tag, TwinStrep-tag and a C-terminal 1D4-tag, and cloned into pcDNA4/TO vector. Single-point mutants were generated for all 360 CB$_2$R residues where non-alanine amino acids were replaced by alanine, and alanines were replaced by valines. For that purpose, PCR with mutation-containing primers was used as described in Heydenreich et al.[52]. Plasmids encoding β-arrestin1-RlucII[53], human GRK2[54], rGFP-CAAX[25,54], and wild-type G$_{\alpha i2}$ protein and an effector protein fused with RlucII (Rap1GAP-RlucII)[28] were previously described. Briefly, for the G protein activation assay, receptor and wild-type G$_{\alpha i2}$ subunit were co-transfected with Rap1GAP-RlucII effector and rGFP-CAAX, while in β-arrestin$_1$ recruitment assay, receptor was co-transfected with β-arrestin1-RlucII, wild-type GRK2, and rGFP-CAAX. In both assays an increase in BRET signal was monitored upon ligand-induced Rap1GAP or β-arrestin recruitment to the plasma membrane.

Transfection

Human embryonic kidney (HEK) 293 T cells[55] were cultured in DMEM, 4.5 g/L glucose, with L-glutamine and phenol red, without sodium pyruvate (#319-015, Wisent Inc., Montreal, Canada), supplemented with 10% Newborn Calf Serum (NCS, iron fortified, #075-350, Wisent Inc., Montreal, Canada) and 1x Penicillin-Streptomycin (PS, #450-201, Wisent Inc., Montreal, Canada) in adherent culture at 37 °C, 5% CO$_2$. For transfection, medium without phenol red was used (#319-051, Wisent Inc., Montreal, Canada). Cells were dissociated using 0.05% Trypsin with 0.53 mM EDTA (#325-142, Wisent Inc., Montreal, Canada) and transiently transfected with receptor and biosensor DNA using 25 kDa linear polyethylenimine (#23966, Polysciences Inc., Warrington, PA, USA) in Cellstar® PS 96-well cell culture plates (Greiner Bio-One, Germany) at a density of 20,000 cells per well.

BRET experiments

Coelenterazine 400a (#340, Prolume Ltd., Pinetop, AZ, USA) was used as the luciferase substrate. HU-210 was purchased from Toronto Research Chemicals (#TRC-H673500, Toronto, ON, Canada) BRET experiments were performed 2 days post-transfection, when culture medium was replaced by 100 µL Tyrode's buffer (137 mM NaCl, 1 mM MgCl$_2$, 1 mM CaCl, 0.9 mM KCl, 3.6 mM NaH, 11.9 mM NaHCO$_3$, 25 mM HEPES, 5.55 mM D-glucose, pH = 7.4). A volume of 0.4 µL of ligand was added to cell plates using a BiomekFX Lab Automation Workstation (Beckman) and a previously calibrated pin tool, followed by incubation at 37 °C for 5 min in a Cytomat 6001 (Thermo Scientific). Coelenterazine 400a working solution (50 µM DBC and 1% Pluronic F-127 in Tyrode's buffer) was added with a Multidrop Combi (Thermo Scientific) to a final concentration of 5 µM and shaken for 10 s. The plates were further incubated for 5 min at room temperature before the BRET signal was read on a Synergy Neo (Biotek) equipped with dual photomultiplier tubes (PMTs) (emission recorded at 410 and 515 nm, gain settings of 150 for each PMT and 1.2 s integration time).

Cell surface ELISA measurements

HEK293T cells were transfected as above using only receptor-coding plasmids in poly-D-lysine-coated 96-well plates and incubated at 37 °C and 5% CO$_2$ for 2 days. Cells were washed with PBS (200 µL/well) and fixed with 3% paraformaldehyde (50 µL/well) for 10 min, followed by three washing steps (100 µL/well, PBS + 0.5% BSA). Receptor was detected by primary rabbit anti-SNAP antibody (50 µL/well of 1:2000

dilution, #A00684, GenScript, 1 h at RT) and anti-rabbit HRP antibody (50 µL/well of a 1:1000 dilution, #NA934, GE Healthcare, 1 h at RT), with washing steps as above, followed by three wash steps with PBS. SigmaFast solution (100 µL/well) was added, followed by incubation at RT protected from light, until color change was observed. To stop the reaction, 25 µL 3 M HCl were added to each well and 100 µL of the solution were transferred to a new transparent 96-well plate for the measurement. The absorbance at 492 nm was measured using a Tecan GENios Plus microplate reader, reporting on the amount of receptor expressed.

Effect of the receptor expression level on maximal ligand-induced response

Receptor titrations were performed to determine the effect of receptor expression level on Emax values of both pathways. Various amounts of CB$_2$R DNA were transfected (0, 0.1, 0.5, 1, 2.5, 5, 10, 25, 50, 100, 150, 200% of the amount used for each biosensor), together with other biosensor components in duplicates. Two days post-transfection one replicate was used to perform ELISA, while the other replicate was used to measure BRET signal upon stimulation with 1 µM HU-210, as described above. Change in BRET signal (Emax) vs. amount of CB$_2$R transfected (percentage of the amount used for each biosensor), and cell-surface expression level (determined by ELISA) vs. amount of CB$_2$R transfected were measured. Correlations of the Emax and ELISA-measured expression levels were determined for each pathway, and data fit equation parameters (linear regression for G$_{\alpha i2}$ activation and non-linear hyperbolic fit for β-arrestin1 recruitment) were used to correct Emax output of each mutant for its previously measured expression level (Supplementary Data 1).

BRET data analysis

The BRET response was determined by the ratio of the light intensity emitted by the acceptor (rGFP, measured at 515 nm), over the light intensity emitted by the BRET donor (RlucII, measured at 410 nm). Single-replicate concentration-response curves were fitted to a Hill equation with a Hill coefficient of 1. For each concentration-response curve, the maximum response of signal (Emax) and the ligand concentration at half-maximal signal response (as pEC50) was determined using the custom software DataFitter (https://github.com/dbv123w/DataFitter), followed by averaging over biological triplicates. For further analysis, Emax of CB$_2$R mutants was corrected for the mutant expression levels and normalized to the WT value (Supplementary Fig. 8), while pEC50 of each mutant was subtracted from the WT value. Both raw and corrected values are reported (Supplementary Data 1).

Model generation and molecular dynamics simulation

As a starting point, we have selected the inactive crystal structure of the CB$_2$R bound to the antagonist AM10257 (PDB code: 5ZTY[31]) as well as the active structure bound to the agonist AM12033 (PDB ID: 6KPF[32]). The sequence of the receptor was reverted to the canonical human sequence using data from UNIPROT [P34972]. Residues between positions 222 and 235 of the ICL3 were removed and endings were capped using ACE and CT3 terminal patches following the GPCRm standard protocol[20]. According to this protocol, experimentally unresolved ICL3 loops that are longer than 10 amino acids are not modeled due to the complication of accurate structural predictions of these highly flexible regions. The approach for this protocol is also based on the observations that GPCRs are able to couple and activate G proteins also in the absence of the ICL3[56]. Nevertheless, to ensure that no artifacts are introduced into TM5 and TM6 dynamics due the lack of ICL3, we carried out a control simulation with the ICL3 modeled. For the ICL3 construction, we used the loop modeling tool and standard settings of the MOE 2022.02 software (Chemical Computing Group). We find that the Root Mean Square Fluctuations (RMSF) of TM5 and TM6 are very similar (Supplementary Fig. 9).

The initial position of the ligand was generated based on the position of the highly similar agonist AM12033 co-solved in the inactive CB$_2$R CryoEM structure (PDB ID: 6KPC[32]) (Supplementary Fig. 10). The resulting complex was embedded in a 54% POPC, 36% POPG and 10% cholesterol membrane, based on the coordinates available in the OPM database[57]. The pre-equilibrated membrane was generated in CHARMM-GUI[58]. Protonation states at a pH of 7.4 were assigned using Propka, and residues facing the membrane were manually curated to avoid charges facing the membrane. The obtained system was solvated with TIP3 waters, and the ionic strength of the solution was maintained at 0.15 M using NaCl ions.

The obtained complex was equilibrated for 100 ns in NPT conditions, with constraints applied to the protein backbone and using the Berendsen barostat[59]. From the equilibrated system, we generated systems for each of the studied mutants (see list in Supplementary Table 1). Every system underwent a short 5 ns NPT equilibration phase to adjust the environment to the introduced mutation. Afterward, we applied a simulation scheme in which each mutant evolved for 1 µs simulation time in an NVT ensemble (Fig. 3B). The last 400 ns were carried out in 5 replicates for the inactive CB$_2$R reaching a total simulation time of 2.6 µs per mutant (i.e, 600 ns plus 5* 400 ns = 2.6 µs). Running multiple independent replicates provides the advantage of sampling different regions of conformational space and enhances results reproducibility (i.e., no enhanced sampling is required)[20,22,60]. In addition, this approach is sufficient to allow the system to comprehensively explore the conformational space around the experimental starting structure which minimizes the dependence on the initial configuration. In addition, we carried out 3 replicates for the active CB$_2$R reaching a total simulation time of 1.8 µs per mutant (i.e, 600 ns plus 3* 400 ns = 1.8 µs).

All simulations were carried out using the ACEMD engine[61]. Parameters were obtained from the Charmm36M forcefield generated in November 2017[62], with ligand parameters generated in Paramchem[63,64] with the CgenFF forcefield[65,66]. The temperature was maintained at 310 K. For NPT runs we have employed a 2 fs timestep, and for NVT runs a 4 fs one. This was possible due to the hydrogen mass repartitioning scheme employed within ACEMD. The reliability and reproducibility checklist for molecular dynamics simulations is found in Supplementary Table 3.

Conservation metrics computation

To calculate the evolutionary conservation score for each residue of the CB$_2$R, we obtained the structural sequence alignment of class A GPCRs from GPCRdb and input it into Capra et al.'s online tool with the Jensen-Shannon Divergence (JSD) scoring method[26]. The default values were used for all parameters, including a window size of 3 and BLOSUM 62 matrices for both the background and target. The JSD measures the similarity between two probability distributions by comparing the distribution of amino acids from a sample in a particular position with the distribution of a set without evolutionary pressure[26]. The JSD ranges from 0 to 1, where 0 indicates identical distributions, and 1 means that the distributions have no overlap. Hence, a JSD score of 1 indicates that the two probability distributions are entirely dissimilar with no common features. We then used conservation scores to investigate the relationship between the impact of mutations on coupling affinities and the evolutionary pressure on each residue. To achieve this, we calculated the ratio of G$_{\alpha i2}$ preferential mutants above each JSD score obtained in the analysis. For example, we found that out of all the residues with a conservation score of 0.36 or higher, 70% are G$_{\alpha i2}$ preferential, compared to the 40% found in the whole sequence. A conservation score distribution of the mutants with a WT-like expression level (80% to 100%) can be found in Fig. 2E. A conservation score distribution for all mutants (independently of the expression level) can be found in Supplementary Fig. 11.

Contacts computation

The contact computation in the simulations was done using the GetContacts package [https://getcontacts.github.io/]. All the interaction types supported by the software were used to compute interaction frequencies. Namely, 3 types of hydrogen bonds, salt bridges, pi-cation, pi-stacking, t-stacking, hydrophobic, Van der Waals including hydrophobic contacts, water bridges and extended water bridges. Each of the interaction types has a set of conditions regarding the distance and relative angle of the two groups involved. The complete specifications of these criteria can be found in the GetContacts repository. After computing the interactions in each frame, the overall contact frequency between pairs of residues was computed. This was achieved by counting all the frames where any contact type was established between two residues and dividing it by the total number of frames of the simulation.

ACN computation

ACN computation. We used the AlloViz v0.1 Python package[67] to construct ACNs for the different simulations and replicas based on the residue contact frequencies. The raw contact frequencies were processed as in Foutch et al.[68] by (1) removing the contacts between consecutive residues in the amino acid sequence, as their interactions are consistently established and provide limited useful information, and (2) defining a lower frequency threshold of 0.1 to filter out contacts that are rarely established. Finally, we built the networks by connecting the pairs of interacting residues (nodes) with edges, weighted by their contact frequency.

Ligand-stabilized ACN (LigACN). Taking the resulting networks from the WT simulations, we used the Dijkstra's algorithm as implemented in NetworkX[69] (https://networkx.org/) to calculate the 100 shortest pathways connecting the ligand CHEMBL5085420 (source) and four selected residues in the intracellular domain of the receptor (sinks) for each replica (Fig. 3B). This resulted in a total of 2000 pathways (100 pathways × 4 sinks × 5 replicas). The sinks, namely Arg131 (3 × 50), Asp240 (6 × 30), Ser303 (8 × 47) and Ser69 (2 × 39), were selected based on their proximity to the G protein in the CB$_2$R-G protein complex (Supplementary Fig. 12). The robustness of this approach was evaluated by assessing the impact of selecting alternative sink residues on the shortest pathways (see Supplementary Fig. 13). Subsequently, we computed the information transmission through each edge in the network as their degeneracy, that is, the frequency with which they appear in the shortest pathways.

Computing the distance to the top connections with highest information transmission (LigACN$_{top}$)

The top connections with highest information transmission (LigACN$_{top}$) are defined setting a degeneracy cutoff ≥ 0.146 (light blue edges in Fig. 3A). Then, we computed the distance of PrefCoup$_{G\alpha i2}$ and Coup$_{G\alpha i2\_\beta arr1}$ mutants to the LigACN$_{top}$ (Fig. 3D). The distance is defined as the number of edges in the shortest path between the mutant residue of interest and any residue from the LigACN$_{top}$. The obtained plot shows that mutants with coupling bias (PrefCoup$_{G\alpha i2}$) are located overall closer to the LigACN$_{top}$ at distances 0 and 1 compared to mutants that behave like the WT receptor (Coup$_{G\alpha i2\_\beta arr1}$). We tested if the proximity of PrefCoup$_{G\alpha i2}$ mutants to the LigACN$_{top}$ was higher than could be expected by chance. For this, we calculate the quantile of the distance of PrefCoup$_{G\alpha i2}$ mutants in the distribution of the distance of random residue sets. Finally, to check for a potential bias by the selected degeneracy cutoff, we also computed the mutant distances for a range of different degeneracy thresholds (0–0.2) which further confirmed our observations (Supplementary Fig. 14).

Definition of a balanced set of CB$_2$R alanine mutants for unveiling the determinants G$_{\alpha i2}$ preferential signaling

We compiled a balanced dataset of Coup$_{G\alpha i2\_\beta arr1}$ and G$_{\alpha i2}$ preferential mutants according to the following criteria: (i) Coup$_{G\alpha i2\_\beta arr1}$ with Emax$_{G\alpha i2}$ and Emax$_{\beta arr1} > 50\%$, (ii) preferential G$_{\alpha i2}$ coupling with an Emax$_{G\alpha i2} > 50\%$ and no measurable arrestin activity (Supplementary Data 1, Supplementary Fig. 15). As cell-surface expression can alter receptor signaling[30], we prioritized the selection of mutants with WT-like expression levels. A final requirement for mutant selection was that mutants are in receptor regions that had been structurally resolved previously to allow their investigations in reliable three-dimensional dynamics models. The final set consists of the wild type and 34 mutants of which 20 were Coup$_{G\alpha i2\_\beta arr1}$ and 14 were G$_{\alpha i2}$ preferring mutants (PrefCoup$_{G\alpha i2}$). The location of selected mutants in the CB$_2$R is indicated in Fig. 4A. Despite the mutant class definition relying exclusively on Emax, it is not ignoring EC50. This is because all the mutants without measurable efficacy also presented a potency of 0. So, independently of which criteria, Emax or EC50, is used, the compositions of the groups would be identical.

Principal component analysis and clustering definition

We conducted a principal component analysis (PCA) on the contact frequencies data in order to reduce its dimensionality and to detect variables that are able to discern between the two mutant groups PrefCoup$_{G\alpha i2}$ and Coup$_{G\alpha i2\_\beta arr1}$. The PCA was constructed using contact frequencies taking into account all residues in the CB$_2$R. The matrix used to calculate the Principal Components (PCs) is 175 ((34 mutants + WT) × 5 replicates) × 4421 (contacts). Then, we explored all 45 pairwise combinations of such components. This inspection revealed the presence of a set of outlier simulations, all of them belonging to the A53V mutant. After the removal of this mutant, we found the best-performing PC plane, defined by PC1 and PC10, by using a Support Vector Classifier (SVC)[70]. The SVC model clearly separates the data into three different clusters for G$_{\alpha i2}$ preferential mutants and one cluster for Coup$_{G\alpha i2\_\beta arr1}$ mutants. Ultimately, we also confirmed this clustering using the K-means algorithm[71].

Cluster characterization

To characterize each cluster, we used logistic regression to differentiate between the wild type-like and the preferential coupling cluster. Because the model could not generalize well with divided training and validation data, we opted to train a regularized model with high bias on the entire dataset. After training, we extracted the coefficients of each predictor variable, sorted them based on absolute value, and selected the top 20 variables. We then associated the coefficient with the residues involved in the interaction that formed the predictor variable. Model and model training was done using the scikit-learn Python module[72]. From all interactions that were highlighted by the highest coefficients in absolute value from the logistic regression we paid special attention to those involving conserved residues and interactions that were densely packed in a specific region of the receptor.

Reporting summary

Further information on research design is available in the Nature Portfolio Reporting Summary linked to this article.

Data availability

Data supporting the findings of this manuscript are available as a Supplementary Information and Supplementary Data 1 to 4. The MD data generated in this study have been deposited in the GPCRmd database under accession code: https://gpcrmd.org/dynadb/publications/1540/. 3D structures used in this study: 6KPC, 5ZTY, 6KPF. Source data are provided with this paper.

Code availability

The python code for data processing is available at GitHub (https://github.com/GPCRmd/prefcoup_cb2r)[73]. Additional data supporting the findings are available from the corresponding authors upon request.

References

1. Rosenbaum, D. M., Rasmussen, S. G. F. & Kobilka, B. K. The structure and function of G-protein-coupled receptors. *Nature* **459**, 356–363 (2009).
2. Maresz, K. et al. Direct suppression of CNS autoimmune inflammation via the cannabinoid receptor CB1 on neurons and CB2 on autoreactive T cells. *Nat. Med.* **13**, 492–497 (2007).
3. Ashton, J. C. & Glass, M. The cannabinoid CB2 receptor as a target for inflammation-dependent neurodegeneration. *Curr. Neuropharmacol.* **5**, 73–80 (2007).
4. Maccarrone, M. et al. Goods and bads of the endocannabinoid system as a therapeutic target: lessons learned after 30 years. *Pharmacol. Rev.* **75**, 885–958 (2023).
5. Tsang, C. C. & Giudice, M. G. Nabilone for the management of pain. *Pharmacotherapy* **36**, 273–286 (2016).
6. Pacher, P., Steffens, S., Haskó, G., Schindler, T. H. & Kunos, G. Cardiovascular effects of marijuana and synthetic cannabinoids: the good, the bad, and the ugly. *Nat. Rev. Cardiol.* **15**, 151–166 (2018).
7. Abu-Sawwa, R., Scutt, B. & Park, Y. Emerging use of Epidiolex (cannabidiol) in epilepsy. *J. Pediatr. Pharmacol. Ther.* **25**, 485–499 (2020).
8. Pandey, P. et al. Determination of the negative allosteric binding site of cannabidiol at the CB1 receptor: A combined computational and site-directed Mutagenesis study. *ACS Chem. Neurosci.* **16**, 311–328 (2025).
9. Tham, M. et al. Allosteric and orthosteric pharmacology of cannabidiol and cannabidiol-dimethylheptyl at the type 1 and type 2 cannabinoid receptors. *Br. J. Pharmacol.* **176**, 1455–1469 (2019).
10. Berger, M., Amminger, G. P. & McGregor, I. S. Medicinal cannabis for the treatment of anxiety disorders. *Aust. J. Gen. Pract.* **51**, 586–592 (2022).
11. Mohammed, S. Y. M. et al. Effectiveness of cannabidiol to manage chronic pain: a systematic review. *Pain. Manag. Nurs.* **25**, e76–e86 (2024).
12. Lowin, T. et al. Cannabidiol (CBD): a killer for inflammatory rheumatoid arthritis synovial fibroblasts. *Cell Death Dis.* **11**, 714 (2020).
13. Di Marzo, V. Targeting the endocannabinoid system: to enhance or reduce?. *Nat. Rev. Drug Discov.* **7**, 438–455 (2008).
14. Smith, J. S., Lefkowitz, R. J. & Rajagopal, S. Biased signalling: from simple switches to allosteric microprocessors. *Nat. Rev. Drug Discov.* **17**, 243–260 (2018).
15. Luttrell, L. M. Minireview: More than just a hammer: ligand 'bias' and pharmaceutical discovery. *Mol. Endocrinol.* **28**, 281–294 (2014).
16. Sivertsen, B., Holliday, N., Madsen, A. N. & Holst, B. Functionally biased signalling properties of 7TM receptors - opportunities for drug development for the ghrelin receptor. *Br. J. Pharmacol.* **170**, 1349–1362 (2013).
17. Morales-Pastor, A. et al. In silico study of allosteric communication networks in GPCR signaling bias. *Int. J. Mol. Sci.* **23**, 7809 (2022).
18. Cao, Y. et al. Unraveling allostery within the angiotensin II type 1 receptor for Gα and β-arrestin coupling. *Sci. Signal.* **16**, eadf2173 (2023).
19. Torrens-Fontanals, M., Stepniewski, T. M., Gloriam, D. E. & Selent, J. Structural dynamics bridge the gap between the genetic and functional levels of GPCRs. *Curr. Opin. Struct. Biol.* **69**, 150–159 (2021).
20. Rodríguez-Espigares, I. et al. GPCRmd uncovers the dynamics of the 3D-GPCRome. *Nat. Methods* **17**, 777–787 (2020).
21. Lopez-Balastegui, M. et al. Relevance of G protein-coupled receptor (GPCR) dynamics for receptor activation, signalling bias and allosteric modulation. *Br. J. Pharmacol.* https://doi.org/10.1111/bph.16495 (2024).
22. Aranda-García, D. et al. Large scale investigation of GPCR molecular dynamics data uncovers allosteric sites and lateral gateways. *Nat. Commun.* **16**, 2020 (2025).
23. Suomivuori, C.-M. et al. Molecular mechanism of biased signaling in a prototypical G protein-coupled receptor. *Science* **367**, 881–887 (2020).
24. Nivedha, A. K. et al. Identifying functional hotspot residues for biased ligand design in G-protein-coupled receptors. *Mol. Pharmacol.* **93**, 288–296 (2018).
25. Namkung, Y. et al. Monitoring G protein-coupled receptor and β-arrestin trafficking in live cells using enhanced bystander BRET. *Nat. Commun.* **7**, 12178 (2016).
26. Capra, J. A. & Singh, M. Predicting functionally important residues from sequence conservation. *Bioinformatics* **23**, 1875–1882 (2007).
27. Pándy-Szekeres, G. et al. GPCRdb in 2018: adding GPCR structure models and ligands. *Nucleic Acids Res* **46**, D440–D446 (2018).
28. Avet, C. et al. Effector membrane translocation biosensors reveal G protein and βarrestin coupling profiles of 100 therapeutically relevant GPCRs. *Elife* **11**, e74101 (2022).
29. Isberg, V. et al. Generic GPCR residue numbers - aligning topology maps while minding the gaps. *Trends Pharmacol. Sci.* **36**, 22–31 (2015).
30. Li, A., Liu, S., Huang, R., Ahn, S. & Lefkowitz, R. J. Loss of biased signaling at a G protein-coupled receptor in overexpressed systems. *PLoS One* **18**, e0283477 (2023).
31. Li, X. et al. Crystal Structure of the Human Cannabinoid Receptor CB2. *Cell* **176**, 459–467.e13 (2019).
32. Hua, T. et al. Activation and signaling mechanism revealed by cannabinoid receptor-G complex structures. *Cell* **180**, 655–665.e18 (2020).
33. Heydenreich, F. M. et al. Molecular determinants of ligand efficacy and potency in GPCR signaling. *Science* **382**, eadh1859 (2023).
34. Oakley, R. H., Laporte, S. A., Holt, J. A., Caron, M. G. & Barak, L. S. Differential affinities of visual arrestin, beta arrestin1, and beta arrestin2 for G protein-coupled receptors delineate two major classes of receptors. *J. Biol. Chem.* **275**, 17201–17210 (2000).
35. Patel, M. et al. Delineating the interactions between the cannabinoid CB2 receptor and its regulatory effectors; β-arrestins and GPCR kinases. *Br. J. Pharmacol.* **179**, 2223–2239 (2022).
36. Bhattacharya, S. & Vaidehi, N. Differences in allosteric communication pipelines in the inactive and active states of a GPCR. *Biophys. J.* **107**, 422–434 (2014).
37. Ma, N., Nivedha, A. K. & Vaidehi, N. Allosteric communication regulates ligand-specific GPCR activity. *FEBS J.* **288**, 2502–2512 (2021).
38. Laine, E., Auclair, C. & Tchertanov, L. Allosteric communication across the native and mutated KIT receptor tyrosine kinase. *PLoS Comput. Biol.* **8**, e1002661 (2012).
39. Rivalta, I. et al. Allosteric communication disrupted by a small molecule binding to the imidazole glycerol phosphate synthase protein-protein interface. *Biochemistry* **55**, 6484–6494 (2016).
40. Hegron, A. et al. Identification of key regions mediating human melatonin type 1 receptor functional selectivity revealed by natural variants. *ACS Pharm. Transl. Sci.* **4**, 1614–1627 (2021).
41. Al-Zoubi, R., Morales, P. & Reggio, P. H. Structural insights into CB1 receptor biased signaling. *Int. J. Mol. Sci.* **20**, 1837 (2019).
42. Morales, P., Goya, P. & Jagerovic, N. Emerging strategies targeting CB cannabinoid receptor: biased agonism and allosterism. *Biochem. Pharmacol.* **157**, 8–17 (2018).

43. Wootten, D., Christopoulos, A., Marti-Solano, M., Babu, M. M. & Sexton, P. M. Mechanisms of signalling and biased agonism in G protein-coupled receptors. *Nat. Rev. Mol. Cell Biol.* **19**, 638–653 (2018).

44. Cong, X. et al. Molecular insights into the biased signaling mechanism of the μ-opioid receptor. *Mol. Cell* **81**, 4165–4175.e6 (2021).

45. Fenalti, G. et al. Molecular control of δ-opioid receptor signalling. *Nature* **506**, 191–196 (2014).

46. Stepniewski, T. M. et al. Mechanistic insights into dopaminergic and serotonergic neurotransmission - concerted interactions with helices 5 and 6 drive the functional outcome. *Chem. Sci.* **12**, 10990–11003 (2021).

47. Kossatz, E. et al. G protein-specific mechanisms in the serotonin 5-HT2A receptor regulate psychosis-related effects and memory deficits. *Nat. Commun.* **15**, 4307 (2024).

48. Martí-Solano, M. et al. Detection of new biased agonists for the serotonin 5-HT2A receptor: modeling and experimental validation. *Mol. Pharmacol.* **87**, 740–746 (2015).

49. Gutkind, J. S. & Kostenis, E. Arrestins as rheostats of GPCR signalling. *Nat. Rev. Mol. Cell Biol.* **19**, 615–616 (2018).

50. Nobles, K. N. et al. Distinct phosphorylation sites on the β(2)-adrenergic receptor establish a barcode that encodes differential functions of β-arrestin. *Sci. Signal.* **4**, ra51 (2011).

51. Gareri, C. et al. Phosphorylation patterns in the AT1R C-terminal tail specify distinct downstream signaling pathways. *Sci. Signal.* **17**, eadk5736 (2024).

52. Heydenreich, F. M. et al. High-throughput mutagenesis using a two-fragment PCR approach. *Sci. Rep.* **7**, 6787 (2017).

53. Quoyer, J. et al. Pepducin targeting the C-X-C chemokine receptor type 4 acts as a biased agonist favoring activation of the inhibitory G protein. *Proc. Natl Acad. Sci. Usa.* **110**, E5088–97 (2013).

54. Beautrait, A. et al. Mapping the putative G protein-coupled receptor (GPCR) docking site on GPCR kinase 2: insights from intact cell phosphorylation and recruitment assays. *J. Biol. Chem.* **289**, 25262–25275 (2014).

55. Beautrait, A. et al. A new inhibitor of the β-arrestin/AP2 endocytic complex reveals interplay between GPCR internalization and signalling. *Nat. Commun.* **8**, 15054 (2017).

56. Rubenstein, R. C., Wong, S. K. & Ross, E. M. The hydrophobic tryptic core of the beta-adrenergic receptor retains Gs regulatory activity in response to agonists and thiols. *J. Biol. Chem.* **262**, 16655–16662 (1987).

57. Lomize, M. A., Pogozheva, I. D., Joo, H., Mosberg, H. I. & Lomize, A. L. OPM database and PPM web server: resources for positioning of proteins in membranes. *Nucleic Acids Res.* **40**, D370–6 (2012).

58. Jo, S., Kim, T., Iyer, V. G. & Im, W. CHARMM-GUI: a web-based graphical user interface for CHARMM. *J. Comput. Chem.* **29**, 1859–1865 (2008).

59. Berendsen, H. J. C., Postma, J. P. M., van Gunsteren, W. F., DiNola, A. & Haak, J. R. Molecular dynamics with coupling to an external bath. *J. Chem. Phys.* **81**, 3684–3690 (1984).

60. Knapp, B., Ospina, L. & Deane, C. M. Avoiding false positive conclusions in molecular simulation: the importance of replicas. *J. Chem. Theory Comput.* **14**, 6127–6138 (2018).

61. Harvey, M. J., Giupponi, G. & Fabritiis, G. D. ACEMD: accelerating biomolecular dynamics in the microsecond time scale. *J. Chem. Theory Comput.* **5**, 1632–1639 (2009).

62. Huang, J. et al. CHARMM36m: an improved force field for folded and intrinsically disordered proteins. *Nat. Methods* **14**, 71–73 (2017).

63. Vanommeslaeghe, K. & MacKerell, A. D. Jr. Automation of the CHARMM General Force Field (CGenFF) I: bond perception and atom typing. *J. Chem. Inf. Model.* **52**, 3144–3154 (2012).

64. Vanommeslaeghe, K., Raman, E. P. & MacKerell, A. D. Jr. Automation of the CHARMM General Force Field (CGenFF) II: assignment of bonded parameters and partial atomic charges. *J. Chem. Inf. Model.* **52**, 3155–3168 (2012).

65. Vanommeslaeghe, K. et al. CHARMM general force field: a force field for drug-like molecules compatible with the CHARMM all-atom additive biological force fields. *J. Comput. Chem.* **31**, 671–690 (2010).

66. Yu, W., He, X., Vanommeslaeghe, K. & MacKerell, A. D. Jr. Extension of the CHARMM General Force Field to sulfonyl-containing compounds and its utility in biomolecular simulations. *J. Comput. Chem.* **33**, 2451–2468 (2012).

67. Nerín-Fonz, F. et al. AlloViz: A tool for the calculation and visualisation of protein allosteric communication networks. *Comput. Struct. Biotechnol. J.* **23**, 1938–1944 (2024).

68. Foutch, D., Pham, B. & Shen, T. Protein conformational switch discerned via network centrality properties. *Comput. Struct. Biotechnol. J.* **19**, 3599–3608 (2021).

69. Hagberg, A. A., Schult, D. A. & Swart, P. J. Exploring network structure, dynamics, and function using NetworkX. In *Proceedings of the Python in Science Conference* 11–15 (SciPy, 2008).

70. Cortes, C. & Vapnik, V. Support-vector networks. *Mach. Learn.* **20**, 273–297 (1995).

71. Lloyd, S. Least squares quantization in PCM. *IEEE Trans. Inf. Theory* **28**, 129–137 (1982).

72. Pedregosa, F. et al. Scikit-learn: machine learning in python. *J. Mach. Learn. Res.* abs/1201.0490, (2011).

73. Morales-Pastor, A., Dieguez-Eceolaza, M. & Selent, J. *Multiple Intramolecular Triggers Converge to Preferential G Protein Coupling in the CB2R.* https://doi.org/10.5281/ZENODO.15270434. (Zenodo, 2025).

74. D'Agostino, R. & Pearson, E. S. Tests for Departure from Normality. Empirical Results for the Distributions of b 2 and √b 1. *Biometrika* **60**, 613 (1973).

75. Hodges, J. L. The significance probability of the Smirnov two-sample test. *Ark. Mat.* **3**, 469–486 (1958).

Acknowledgements

Author contributions

A.M.P., V.L., and T.M.S. carried out the molecular dynamics simulations and data analysis under the supervision of J.S. T.M. carried out the alanine scan for the CB$_2$R under the supervision of D.B.V. and M.B. and the signaling assays under the supervision of M.B. and D.B.V. F.M.H., B.P., and J.D. contributed to data collection. C.L.G. designed some of the biosensors used in this study. T.F. contributed to the initial data analysis. W.G., A.C.R., and U.G. participated in ligand selection for the alanine scanning signaling screen and provided unique CB$_2$-selective compounds. D.B.V. wrote the DataFitter software for high-throughput data analysis. D.A.S., C.N., and E.J.K. validated the dependence of arrestin recruitment on GRK-mediated receptor phosphorylation. A.M.P. and J.S. wrote the manuscript. T.M. and D.B.V. contributed to the manuscript writing. M.D.E. carried out major manuscript revision including

additional data analysis, representation and discussion under the supervision of J.S. All authors revised the manuscript. D.B.V. and J.S. supervised and coordinated the whole project.

Competing interests

M.B. is the president of the Scientific Advisory Board of Domain Therapeutics, a biotech company to which biosensors used in this study were licensed for commercial use. D.B.V. is founder of Z7 Biotech Ltd, an early-stage drug discovery contract research organization. All other authors declare no competing interests.

Additional information

Supplementary information The online version contains supplementary material available at https://doi.org/10.1038/s41467-025-60003-0.

Correspondence and requests for materials should be addressed to Dmitry B. Veprintsev or Jana Selent.

Peer review information *Nature Communications* thanks Nadine Jagerovic who co-reviewed with Paula MoralesArnau Cordomí, Francesco Raimondi and the other, anonymous, reviewer(s) for their contribution to the peer review of this work. A peer review file is available.

Reprints and permissions information is available at http://www.nature.com/reprints

Publisher's note Springer Nature remains neutral with regard to jurisdictional claims in published maps and institutional affiliations.